ACSNANO

www.acsnano.org

ARTICLE

Surface Ligand Modification on Ultrathin $Ni(OH)_2$ Nanosheets Enabling Enhanced Alkaline Ethanol Oxidation Kinetics

Ziyi Zhang, Yutao Dong, Corey Carlos, and Xudong Wang*

Cite This: *ACS Nano* 2023, 17, 17180–17189

Read Online

ACCESS | Metrics & More | Article Recommendations | Supporting Information

ABSTRACT: The ethanol oxidation reaction (EOR) is an economical pathway in many electrochemical systems for clean energy, such as ethanol fuel cells and the anodic reaction in hydrogen generation. Noble metals, such as platinum, are benchmark catalysts for EOR owing to their superb electrochemical capability. To improve sustainability and product selectivity, nickel (Ni)-based electrocatalysts are considered promising alternatives to noble-metal EOR. Although Ni-based electrocatalysts are relieved from intermediate poisoning, their performances are largely limited by their relatively high onset potential. Therefore, the EOR usually competes with the oxygen evolution reaction (OER) at working potentials, resulting in a low EOR efficiency. Here, we demonstrate a strategy to modify the surface ligands on ultrathin $Ni(OH)_2$ nanosheets, which substantially improved their catalytic properties for the alkaline EOR. Chemisorbed octadecylamine ligands could create an alcoholophilic layer at the nanosheet surface to promote alcohol diffusion and adsorption, resulting in outstanding EOR activity and selectivity over the OER at higher potential. These non-noble-metal-based 2D electrocatalysts and surface ligand engineering showcase a promising strategy for achieving high-efficiency electrocatalysis of EOR in many practical electrochemical processes.

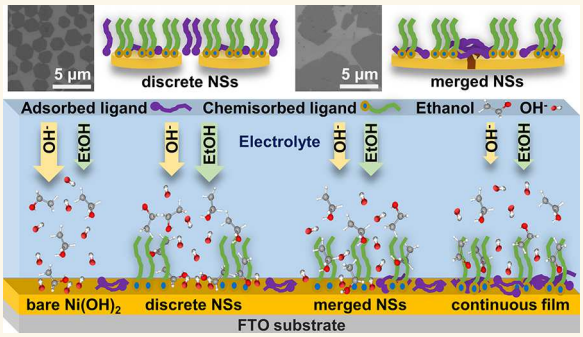

KEYWORDS: *2D materials, non-noble-metal-based catalyst, ethanol oxidation reaction, ionic layer epitaxy, surface modification, catalytic kinetics*

INTRODUCTION

Ethanol is an abundant renewable energy source for direct fuel cells with high energy density, low emission, and safety for storage.[1] For decades, considerable research efforts have been devoted to developing highly efficient catalysts for the ethanol oxidation reaction (EOR) to alleviate the increasing environmental pollution and fossil fuel consumption.[2] Because electrochemical ethanol oxidations usually have lower working potentials at the anode compared to that of oxygen evolution reactions (OERs), it is considered a more viable anode reaction to be paired with hydrogen evolution reactions in electrochemical and photoelectrochemical systems.[3] To date, the best-performing catalysts for EORs are Pt-based materials, despite their high costs.[4] However, the intermediate poisoning issue[5] remains a crucial challenge that limits the application potential of noble-metal-based catalysts for EORs.[6−15] Therefore, developing efficient non-precious-metal catalysts for EORs has become one of the most important topics in renewable energy.

Among all the proposed materials, Ni is the most promising to replace noble metals for the EOR owing to its much lower cost, no poisoning effect, and high selectivity to oxidizing alcohols into their corresponding carboxyl acids with a hydride transfer (HydT) mechanism.[16−22] However, a big challenge for Ni-based materials is that the EOR usually competes with the OER at the anode surface, because the alkaline EOR also involves hydroxide ions (OH^-).[3,17] Reducing either alcohol or OH^- concentrations will suppress the EOR performance.[22] Owing to their structural advantages, 2D nanomaterials are commonly recognized as highly efficient catalysts.[2,23,24] Here, we show a substantially improved EOR from ultrathin $Ni(OH)_2$ nanosheets (NSs) by tuning the surface adsorption rate between alcohol molecules and OH^-. We utilized amphiphilic octadecylamine (ODAM) ligands to modify the

Received: June 4, 2023
Accepted: August 30, 2023
Published: September 1, 2023

https://doi.org/10.1021/acsnano.3c05014
ACS Nano 2023, 17, 17180−17189

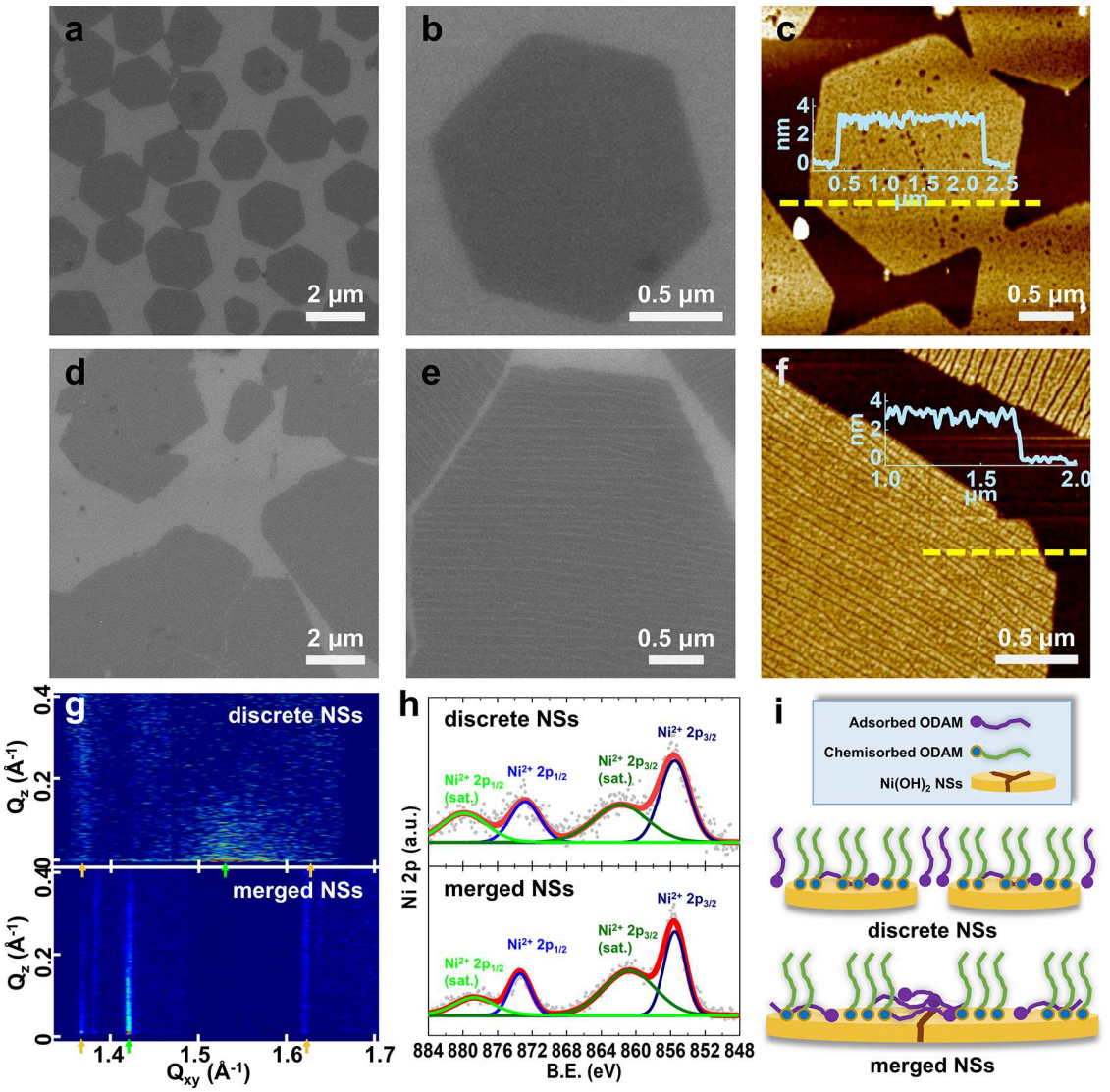

Figure 1. $Ni(OH)_2$ NS characterizations. (a, b) SEM images and (c) AFM topography of discrete NSs. (d, e) SEM images and (f) AFM topography of merged NSs. (g) Grazing incidence X-ray diffractions of $Ni(OH)_2$ NSs. (h) XPS Ni 2p spectra of $Ni(OH)_2$ NSs. (i) Schematic illustration of the $Ni(OH)_2$ NSs surface structures with ODAM ligands.

surface of ultrathin $Ni(OH)_2$ NSs via ionic layer epitaxy (ILE).[25−27] The ligands chemisorbed onto the NS surface can generate an alcoholophilic layer at the catalyst−electrolyte interface, leading to more favorable selective sorption[28−30] of alcohol molecules on the catalyst surface to enhance the EOR in competition with OER, resulting in more efficient alcohol oxidation. This result demonstrated a promising approach for improving the EOR selectivity in competition with the the OER by tuning the catalyst surface chemistry through rational ligand modification. It can be further applied to many other types of electrolysis systems, where the reactants have different polarities.

RESULTS AND DISCUSSION

The $Ni(OH)_2$ NSs were synthesized via a typical ILE approach[25,26,31−33] in glass vials. Freestanding discrete NSs grew from 4 h synthesis at the interface between air and an aqueous solution containing 2.5 mM $NiCl_2$ and 2 mM $(NH)_2$tartrate with a cationic protonated ODAM monolayer (1.59 nmol cm^{-2}) on the solution surface. The ODAM monolayer attracts Ni^{2+} to the interface to form 2D crystals within a self-confined double-layer region.[34−36] Introducing tartrate ions in the solution could form coordinated Ni^{2+}, preventing the nucleation in bulk solution.[37−39] As the scanning electron microscopy (SEM) images show in Figure 1a,b, the hexagonal $Ni(OH)_2$ NSs assembled at the air−water interface had a uniform morphology with an average lateral size of 2 μm. In some high-packing-density regions, some attaching NSs also merge along their edges. The AFM topographic scan (Figure 1c) shows a uniform NS thickness of 3.3 nm, with a roughness of 0.2 nm. The joint part connecting two NSs had a smooth flat surface without kinks. There were a few pinhole defects on the surface of the NS which were induced by the disorder in the surfactant monolayer.[27] To achieve large-area NS coverage, this merging phenomenon was further facilitated by increasing the precursor concentration and extending the synthesis period (Figure S1). 5 mM $NiCl_2$ and 4 mM $(NH)_2$tartrate produced merged NSs with sizes of tens of micrometers (Figure 1d−f). Similar to the discrete NSs, the merged NSs all had sharp facets and a uniform flat top surface with the same thickness of 3.3 nm. In addition, there were

https://doi.org/10.1021/acsnano.3c05014
ACS Nano 2023, 17, 17180−17189

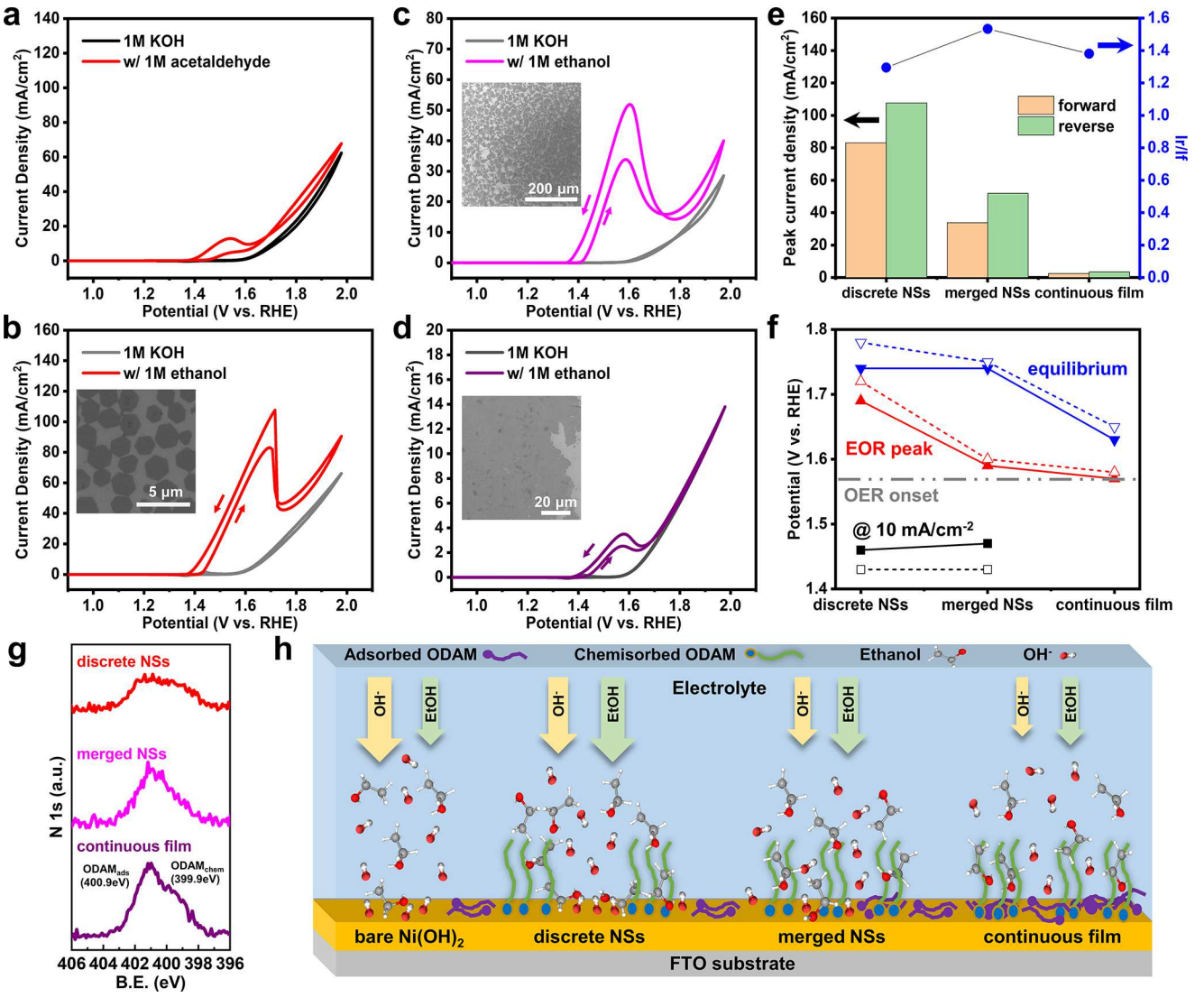

Figure 2. (a) CV curves of discrete $Ni(OH)_2$ NSs in a 1 M KOH aqueous solution without and with 1 M acetaldehyde. CV curves of (b) discrete, (c) merged, and (d) continuous $Ni(OH)_2$ NSs in 1 M KOH aqueous solution without and with 1 M ethanol. Insets are the SEM images of the corresponding NSs (CV scan rate: 50 mV s^{-1}). (e) Summary of the EOR peak current densities of $Ni(OH)_2$ NSs. (f) Summary of the critical potentials in CV curves from forward (solid) and reverse (dashed) scans. (g) XPS N 1s spectra of $Ni(OH)_2$ NSs. (h) Schematic diagram of possible chemical environments at the electrolyte−$Ni(OH)_2$ NSs interface.

obvious grain boundaries on the merged NS surfaces between different domains. The orientation of each domain could be identified by a "tiger-skin" like surface feature. These parallel trenches had an average width of 12 nm and an average separation of 40 nm. This surface feature may be caused by the Oswald ripening and strain relaxation during the merging of small NSs.[27] A continuous NS film with the same merged structure was obtained at a higher ODAM concentration of 4.77 nmol cm^{-2} and an extended synthesis time of 6 h (Figure S1d−f).

In situ grazing incidence X-ray diffraction was used to characterize lateral ordering structures at the air−water interface. As shown in Figure 1g and Figure S2, the ODAM monolayer on deionized water exhibits a packing spacing of 4.18 Å, corresponding to the diffraction peak at 1.504 $Å^{-1}$. With the presence of precursor ions in the solution, an electrical double layer forms in the early incubation period and rearranges the ODAM packing to 1.528 and 1.431 $Å^{-1}$ for $NiCl_2$ concentrations of 2.5 and 5 mM, respectively. After ~45 min, diffraction peaks at 1.376 and 1.624 $Å^{-1}$ appeared, which could be assigned to the (110) and (100) planes of β-$Ni(OH)_2$ with (3×3)R30 reconstruction, respectively.[40,41] The elemental states of the $Ni(OH)_2$ NSs were studied by X-ray photoelectron spectroscopy (XPS). Both the discrete and merged NSs had Ni $2p_{3/2}$ and $2p_{1/2}$ peaks at 855.6 and 873.0 eV, respectively, without multiplet-splits, indicating the valence state of Ni^{2+} in $Ni(OH)_2$ (Figure 1h).[42] XPS N 1s spectra also identified a composition change of ODAM ligands as the NSs merged (Figure S3). The two characteristic peaks at 400.9 and 399.9 eV were assigned to the adsorbed cationic protonated amine ($ODAM_{ads}$) and the chemisorbed amine ($ODAM_{chem}$), respectively.[43] The intensity of $ODAM_{ads}$ increased when merging of NSs developed. This suggests that during ILE synthesis, the excess protonated ODAM molecules between discrete NSs might be pushed onto the NS surface during the merging process. Figure 1i gives the schematic surface structures of the ultrathin $Ni(OH)_2$ NSs with ODAM as capping ligands and the roles of $ODAM_{chem}$ and $ODAM_{ads}$.

https://doi.org/10.1021/acsnano.3c05014
ACS Nano 2023, 17, 17180−17189

$Ni(OH)_2$ crystals nucleate at the interfacial electrical double layer and grow epitaxially, directed by the chemisorbed ODAM ligands. The highly movable discrete NSs at the interface rearrange and connect into a large NS. As the NSs merged together, they might break the ODAM assembling between NS and squeezed them tightly. As a result, excess protonated ODAM molecules may be pushed to the NS surfaces and be physically adsorbed there, especially near the merging boundaries.

The detailed reaction mechanisms of the alcohol oxidation reaction on $Ni(OH)_2$ have been well studied by Choi's group,[17,18] and we used the electrochemical methods to study the EOR catalytic performance and mechanisms of our $Ni(OH)_2$ NSs. The as-synthesized NSs were transferred onto fluorine-doped tin oxide (FTO) substrates and were investigated in 1 M KOH electrolytes without and with 1 M organic compounds. Here, acetaldehyde and ethanol were used to provide comparative insights. The bare FTO substrate shows negligible catalytic effects for these oxidation reactions (Figure S4). The discrete $Ni(OH)_2$ NSs were converted to NiOOH before the onset potential of the OER, within the range between 1.41 and 1.52 V vs RHE (Figure S5). Due to the ultrathin 2D structure, the $Ni(OH)_2$ NSs exhibited a high catalytic activity for the OER, giving a current density of 10 mA cm^{-2} at an overpotential of 440 mV. There are two common EOR mechanisms for Ni-based catalysts: (1) indirect mechanism with hydrogen atom transfer (HAT) at Ni^{3+} active sites[44−46] and (2) potential-dependent mechanism with hydride transfer (HydT) at Ni^{4+} active sites.[17,18] Cyclic voltammetry (CV) (Figure 2a,b) and electrochemical impedance spectroscopy (EIS) (Figure S6) were applied to evaluate the contributions of these two mechanisms in $Ni(OH)_2$ NS catalysis. The CV curves exhibited a characteristic shape with an oxidation peak corresponding to oxidation of the organic species, followed by a current rise corresponding to water oxidation. The aldehyde oxidation peaked at 1.52 V, which was within the Ni^{2+}/Ni^{3+} conversion potential range and showed only modest enhancement at more positive bias (Figure 2a). This suggests that oxidation of aldehyde was mainly contributed by the indirect HAT mechanism.[17,46] The OER became dominant after the onset potential of 1.57 V. The EIS measured at 1.45 V revealed the slow reaction kinetics of the indirect mechanism in aldehyde oxidation (Figure S6a). In parallel, the current density of ethanol oxidation kept increasing and reached a peak value of 78.2 mA cm^{-2} at 1.70 V (Figure 2b). Beyond 1.52 V, the potential-dependent mechanism became dominant with more active HydT at Ni^{4+} sites.[17] The EISs measured at 1.45 and 1.57 V reveal that HydT has faster kinetics than HAT (Figure S6b). The results from measurements demonstrated that HydT is the most effective mechanism in the potential-dependent oxidation of ethanol, which was consistent with the result of the mechanism studies of alcohol oxidation on $Ni(OH)_2$ catalyst reported by the Choi group.[17,18] The EOR was even more active than the OER until 1.72 V, where a new equilibrium between the EOR and the OER was achieved. Under higher applied bias, the OER became more energy favorable and dominated the electrochemical process. The current density of ethanol oxidation was only slightly enhanced compared with that of water oxidation. The CV curves measured without and with ethanol were nearly parallel in the dominant region of the OER, suggesting that Ethe OR had an almost constant rate dependent on the potential. Therefore, the ethanol oxidation CV curve can be divided into two segments separated by the equilibrium potential: the EOR-dominant region, driven by the HydT potential-dependent mechanism, and the OER-dominant region. The largely enhanced EOR region from $Ni(OH)_2$ NSs could be attributed to the ultrathin 2D structure that provides a rapid charge transfer to maintain the high valence states of Ni allowing highly effective HydT.

To further investigate the morphology influences on the EOR catalytic properties of our $Ni(OH)_2$, the same set of electrochemical measurements were conducted on discrete, merged, and continuous NSs. CV curves in Figure 2b−d present the EOR catalytic performance of all $Ni(OH)_2$ NSs in an alkaline environment. Without ethanol, all three $Ni(OH)_2$ NSs exhibited similar catalytic effects for the OER with an onset potential of 1.57 V vs RHE. Among all morphologies, discrete NSs demonstrated the highest activity. The overpotentials at 10 mA cm^{-2} for discrete, merged, and continuous $Ni(OH)_2$ NSs were 440, 580, and 670 mV, respectively. With additional 1 M ethanol in the electrolyte, they all had an EOR onset potential of 1.4 V vs RHE, which was 170 mV lower than that of the OER. The overpotentials at 10 mA cm^{-2} in the forward scan direction were 230, 240, and 670 mV for discrete, merged, and continuous NSs, respectively. They all showed an enhanced HydT mechanism with peak current densities from the reverse scan direction of 107.7, 51.9, and 3.5 mA cm^{-2} for discrete, merged, and continuous NSs, respectively (Figure 2e and Figure S7). In the OER-dominant region, the CV curves of continuous NSs overlapped with and without ethanol. They showed almost no enhancements with ethanol presence. Comparatively, discrete and merged morphologies showed large EOR enhancements. The current densities of discrete and merged NSs increased to 24 and 12 mA cm^{-2}, respectively. Furthermore, the discrete morphologies of NSs demonstrated a superior ability to promote the EOR in several aspects (Figure 2f). In addition to the enhanced current density, the EOR-dominant region of the discrete NSs also extended to a more positive bias, with the peak shifting closer to the corresponding equilibrium potential. This suggests that the reaction kinetics were faster in discrete NS morphologies, leading to a more rapid EOR to OER conversion and a relatively higher EOR enhancement. Overall, discrete NSs gave the greatest enhancement for the EOR on the potential-dependent HydT mechanism with the largest EOR-dominant region, highest peak activity, and fastest electrocatalytic kinetics. The discrete NSs postpone the EOR- to OER-dominant conversion potential to 1.78 V, which is 210 mV higher than the onset potential of the dominant conversion potential of the OER onset potential. The EOR performance of the $Ni(OH)_2$ NSs was compared with those of other non-noble-metal-based electrocatalysts (Figure S8 and Table S1). With the superior ultrathin 2D morphology and the enhanced effect from the surface ligand modification, the activities of the discrete $Ni(OH)_2$ NSs stand at the frontier of similar materials from the literature.

To understand the origin of the outstanding EOR performance from the discrete NSs, we analyzed the surface structure difference between the $Ni(OH)_2$ NSs. As the XPS N 1s spectra show in Figure 2g, there were two types of interactions between ODAM ligands and NS surfaces, i.e. physically adsorbed ($ODAM_{ads}$, 400.9 eV) and chemisorbed ($ODAM_{chem}$, 399.9 eV). According to the NS characterizations, we discovered that excess ODAM molecules were accumulatively adsorbed on the NS surface during the merging

https://doi.org/10.1021/acsnano.3c05014
ACS Nano 2023, 17, 17180−17189

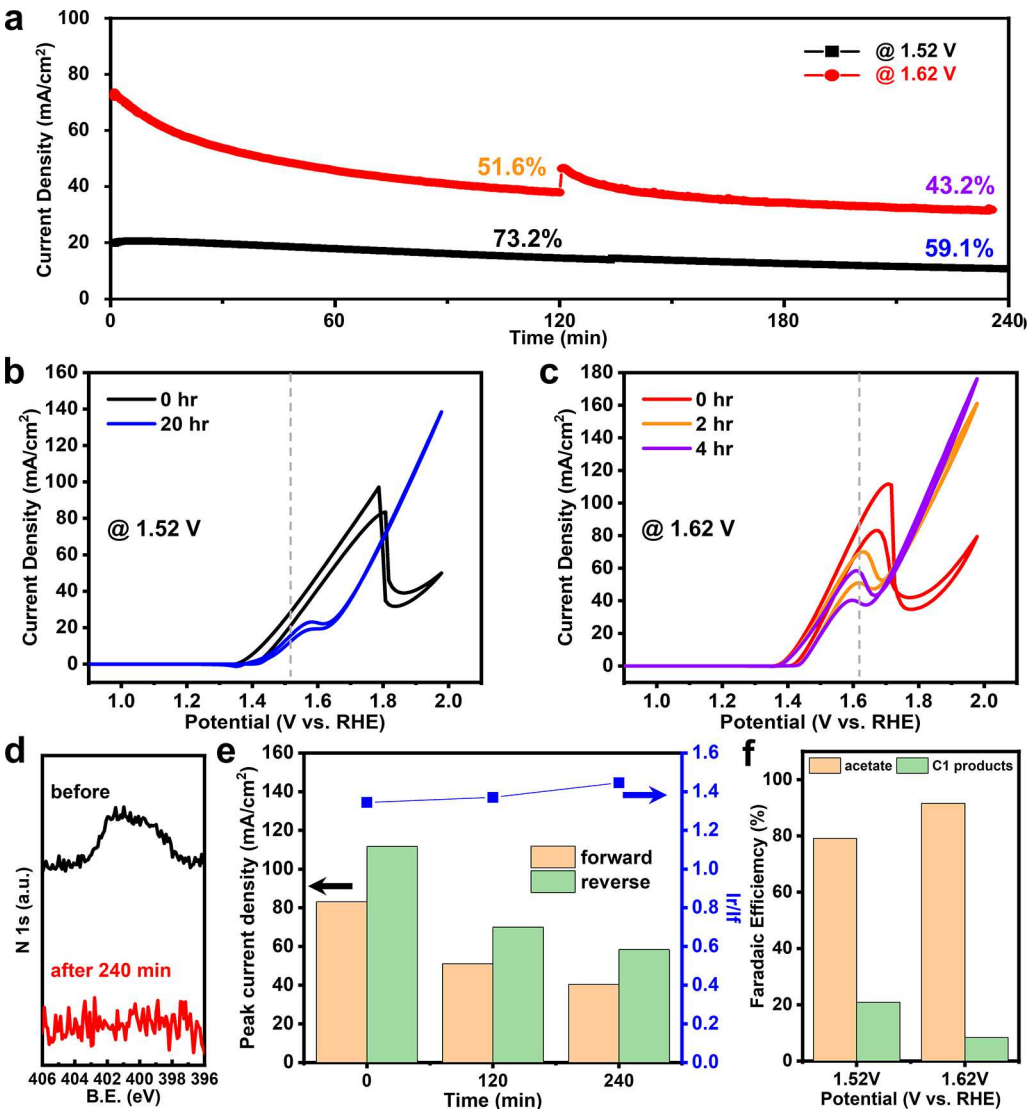

Figure 3. (a) Long-term stability with CA curves of discrete $Ni(OH)_2$ NSs in 1 M KOH aqueous solution with 1 M ethanol at 1.52 and 1.62 V vs RHE. (b) CV curves measured before the test and after a 20 h test at 1.52 V. (c) CV curves measured before the test and after 2 and 4 h tests at 1.62 V (CV scan rate: 50 mV s^{-1}). (d) XPS N 1s spectra of NSs before and after the 4 h test. (e) Summary of the EOR peak current densities. (f) Faradaic efficiency of ethanol oxidation products.

process. The schematic diagram in Figure 2h illustrates the possible chemical environments at the electrolyte−$Ni(OH)_2$ NSs interface during the EOR. The bare $Ni(OH)_2$ surface is less alcoholophilic[47,48] but more hydrophilic.[49−51] $ODAM_{chem}$ ligands anchored on the $Ni(OH)_2$ NS surface during the ILE growth, and their hydrophobic tails were likely stretched to form a more alcoholophilic layer near the catalyst surface to improve the surface-selective sorption of ethanol.[28,30] On the other hand, the $ODAM_{ads}$ molecules were more randomly adsorbed among the anchored $ODAM_{chem}$ ligands, likely blocking the catalytically active sites. Discrete NSs were mostly covered with $ODAM_{chem}$ and thus had the most alcoholophilic surfaces[29] that were favorable for alcohol adsorption[28] and EOR kinetics. Although merged and continuous NSs also have rich active catalytic sites on their surfaces, the higher coverage of excess $ODAM_{ads}$ would significantly suppress the electrochemical reactions.

As the best-performing EOR catalyst, the long-term EOR performance of discrete $Ni(OH)_2$ NSs was carried out at 1.52 and 1.62 V corresponding to the HAT and HydT mechanisms. The results of 4 h chronoamperometric (CA) tests are presented in Figure 3a. At 1.52 V, the current density remained at 73.2% and 59.1% after 2 and 4 h. After running the test for 20 h, $Ni(OH)_2$ NSs were still highly active but became a good catalyst for the OER. After 20 h, the EOR peak decreased dramatically, and the current density at 1.95 V increased by ∼3 times from its initial value (Figure 3b). A stability test at 1.62 V further showed that the current density retained 51.6% and 43.2% of its initial value after 2 and 4 h, respectively. After 4 h, small bubbles could be observed on the working electrode (Videos S1 and S2), indicating the formation of the O_2 gas. This phenomenon suggested that the catalytic kinetics gradually transitioned from the EOR to a dominant OER during the long-period test, which may be induced by the $ODAM_{chem}$ ligand stripping during the test.

The EOR to OER transition could be clearly illustrated by changes in the corresponding CV curves (Figure 3c). After 2 h, the current density in the OER-dominant region markedly increased and the EOR peak slightly decreased to a lower potential range. After 4 h, the current density did not change in

https://doi.org/10.1021/acsnano.3c05014
ACS Nano 2023, 17, 17180−17189

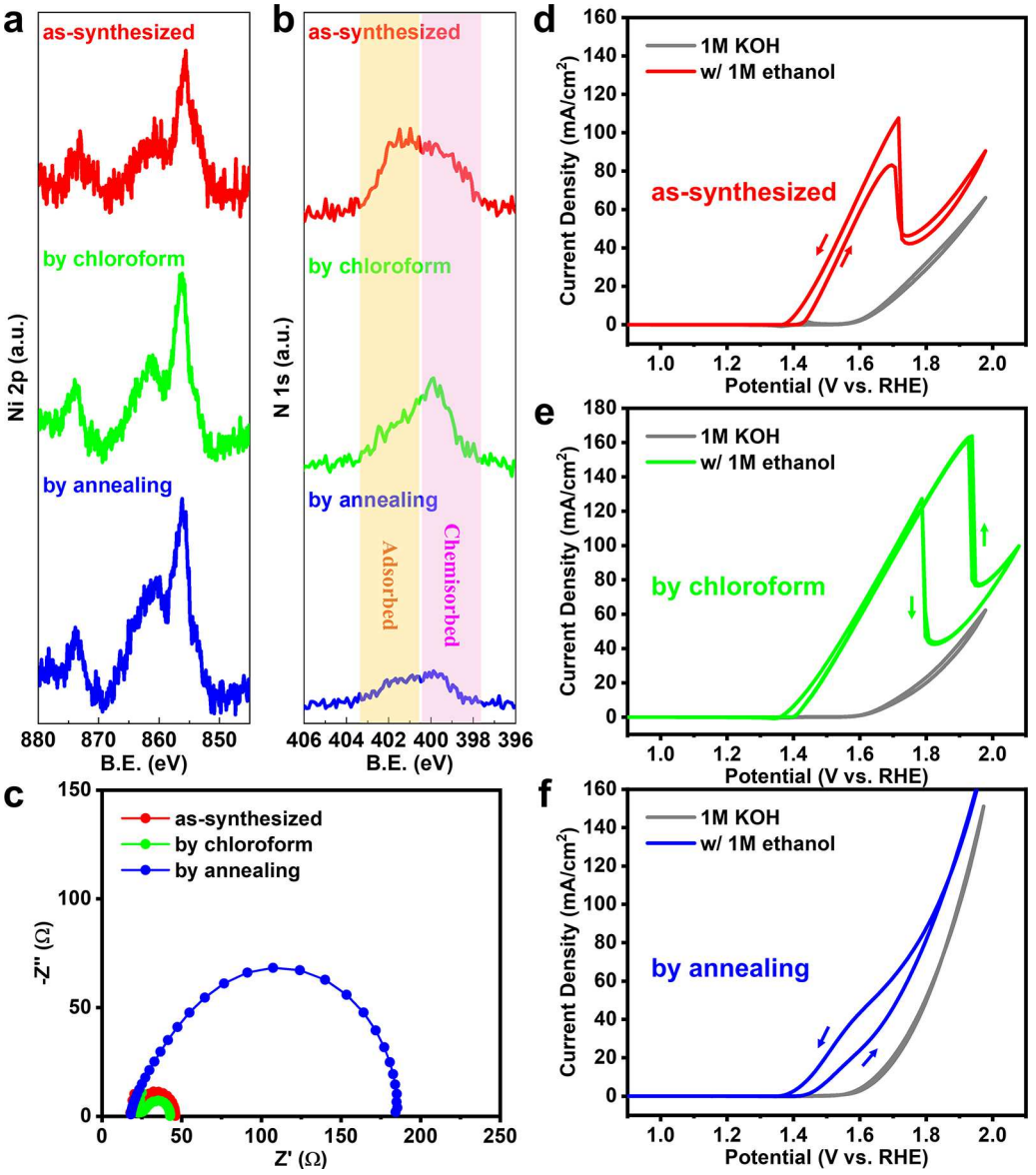

Figure 4. XPS (a) Ni 2p and (b) N 1s spectra of discrete $Ni(OH)_2$ NSs with different surface treatments. (c) Nyquist plots of discrete $Ni(OH)_2$ NSs for ethanol oxidation with different surface treatments in 1 M KOH aqueous solution without and with 1 M ethanol (measured at 1.57 V vs RHE). CV curves of surface-treated discrete $Ni(OH)_2$ NSs: (d) as-synthesized; (e) by chloroform; (f) by annealing for 1 h at 200 °C in N_2 flow (CV scan rate: 50 mV s^{-1}).

the OER-dominant region and the EOR peak was further reduced. The first 2 h current density increase in the dominant region of the OER could be attributed to the exposure of Ni active sites as a result of removing $ODAM_{ads}$. The stripping of $ODAM_{chem}$ was relatively slow, as reflected by the EOR peak decreasing during the 4 h test. The current density was almost stabilized after 4 h, suggesting all $ODAM_{chem}$ ligands were detached. SEM and XPS were also used to characterize the NS before and after the 4 h stability test (Figure 3d and Figure S9). The morphology and Ni chemical state of discrete $Ni(OH)_2$ NSs did not change after the 4 h electrochemical reactions. The XPS N 1s spectra confirmed that ODAM has been fully removed from the NS surface after 4 h. The peak current density ratio between reverse and forward scans was well preserved (Figure 3e), suggesting that the HydT kinetics for the EOR were unchanged over time. The electrolysis products from the HAT and HydT mechanisms were analyzed by ^1H NMR (Figure 3f and Figure S10). The conversion selectivity of ethanol to acetate was 79.1% at 1.52 V (HAT) and 91.6% at 1.62 V (HydT). Discrete $Ni(OH)_2$ NSs with HydT in the potential-dependent mechanism were highly efficient and selective for ethanol to acetate, as desired.

To further prove the proposed EOR enhancement mechanism, two additional surface treatment approaches were applied to discrete $Ni(OH)_2$ NSs. The as-prepared FTO-supported NSs were either thoroughly rinsed by chloroform or by annealing for 1 h at 200 °C in N_2 flow. The EOR performances of these surface-treated NSs were characterized and compared. The hexagonal $Ni(OH)_2$ NS morphology and the chemical state of Ni were both well preserved after treatment with chloroform or annealing (Figure 4a and Figure S11). Only the ODAM ligands were changed by these treatments (Figure 4b). Chloroform rinsed off most $ODAM_{ads}$ without removing $ODAM_{chem}$, whereas both types of

https://doi.org/10.1021/acsnano.3c05014
ACS Nano 2023, 17, 17180−17189

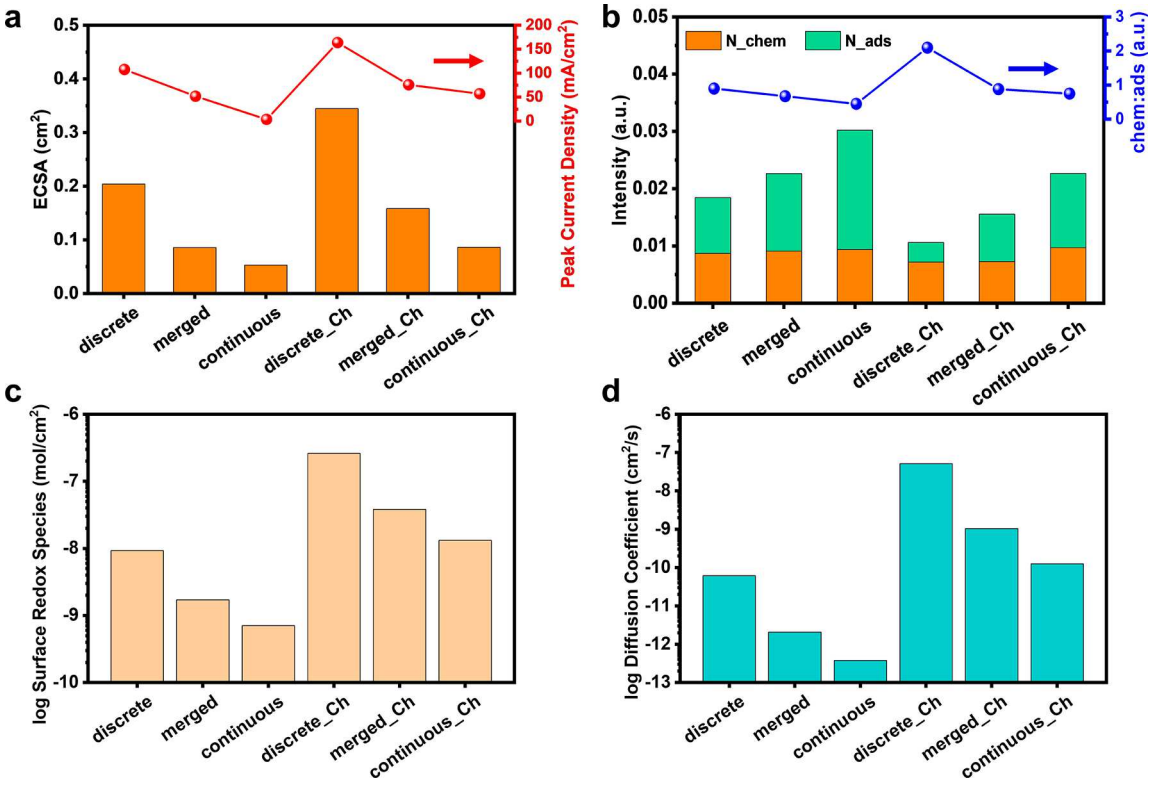

Figure 5. (a) Calculated ECSAs of $Ni(OH)_2$ NSs from double-layer capacitance. (b) Nitrogen from two types of ODAM ligands, (c) surface coverages of redox species, and (d) diffusion coefficients of $Ni(OH)_2$ NSs.

ODAMs could be removed by annealing. The EIS results measured at 1.57 V in 1 M KOH with 1 M ethanol showed a large resistance increase of the NSs after annealing, while the resistance of chloroform-treated NSs was only slightly decreased (Figure 4c). The changes in CVs of these surface-treated NSs agreed well with the mechanisms discussed above (Figure 4d–f and Figure S12). The chloroform treatment further increased the current density, with a wider EOR-dominant region. However, the performance of the OER was not significantly influenced. This change confirmed that $ODAM_{chem}$ was directly related to the improved EOR catalytic performance. On the other hand, annealed NSs gave a smaller EOR peak with a smaller EOR-dominant region. Nevertheless, the OER activity was greatly promoted, as evidenced by the almost doubled current density in the OER-dominant region. This observation suggested that when both types of ODAMs were removed, although more active sites were exposed, the OER was more favorable than the EOR on the bare $Ni(OH)_2$ NS surface. Additional experiments tested at different ethanol concentrations also led to the same conclusions (Figures S13 and S14). The enhancing effect from $ODAM_{chem}$ is the same as the increasing ethanol concentration in the electrolyte. As a result, the promotion of potential-dependent HydT EOR was evidenced by a wider EOR-dominant region and a higher peak activity.

To better understand the difference of the surface active area in the NSs, we performed CV measurements at different scan rates in the non-Faradaic region to estimate the electrochemically active surface area (ECSA) of all $Ni(OH)_2$ NSs (Figure 5a and Figures S15 and S16) and compared the results with the nitrogen oxidation state analyses from the corresponding XPS spectra (Figure 5b and Figures S17 and S18). The ESCAs of the discrete, merged, and continuous NS morphologies are 0.204, 0.0857, and 0.0530 cm^2, respectively. Compared to the trench-rich morphologies (merged and continuous), the discrete NSs with fewer edges exhibited the highest ECSA, suggesting that the surface was more active than the edges in the ultrathin layered $Ni(OH)_2$ structure.[17,52] After fitting the XPS N 1s spectra, we evaluated the changes of the chemisorbed (399.9 eV) and adsorbed (400.9 eV) ligands on these NSs before and after chloroform treatment (Figure 5b). The intensity of the N 1s peak of adsorbed ODAM moderately decreased in all three sizes, while the intensity of the N 1s peak of chemisorbed ODAM only marginally dropped. Since XPS peak intensities of Ni were almost consistent (Figure S19), the N peak intensity analysis revealed that chloroform rinsing was effective for removing adsorbed ODAM from all types of NS surfaces. The chloroform treatment raised the NSs' ECSA to 0.345, 0.0862, and 0.0150 cm^2, respectively. The discrete morphology exhibited the greatest enhancement and still had the highest ECSA among the three morphologies. The ECSA benefited from more surface site exposure after the removal of adsorbed ligands. The EOR peak current density was related to the ECSA (Figure 5a and Figure S20), where ethanol oxidation reached its maximum when all active sites were occupied with a potential-dependent mechanism. The chemisorbed ligands were critical to creating an alcoholophilic layer for maintaining favorable EOR kinetics at higher potentials. Removing adsorbed ligands not only exposed more active areas for a higher maximum EOR activity but might also modulate the ethanol diffusion on the electrolyte side.

CV measurements were also conducted at different scan rates in the Ni^{2+}/Ni^{3+} redox region to estimate the surface coverages of redox species and diffusion coefficients of $Ni(OH)_2$ NSs[53−57] (see details in Methods and Figures S21−S23). It was found that the surface coverages of $Ni^{2+}/$

https://doi.org/10.1021/acsnano.3c05014
ACS Nano 2023, 17, 17180−17189

Ni^{3+} redox species of the discrete, merged, and continuous NSs were 9.27×10^{-9}, 1.70×10^{-9}, and 7.04×10^{-10} mol/cm^2, respectively (Figure 5c). After removing the adsorbed ligands by chloroform treatment, the values of this coverage were enhanced to 2.60×10^{-7}, 3.82×10^{-8}, and 1.32×10^{-8} mol/cm^2 for the discrete, merged, and continuous NSs, respectively. The surface coverage of the Ni^{2+}/Ni^{3+} redox species showed a strong relationship to the ECSA (Figure 5a), which was determined by the amount of adsorbed ligand (Figure 5b). With a similar level of chemisorbed ligands on the NS surface, with less coverage of the adsorbed ligands, a larger active area was exposed, and the higher surface coverage of Ni^{2+}/Ni^{3+} redox species was measured. The proton diffusion coefficients showed a variation trend similar to that of the surface coverage of redox species (Figure 5d). The values of the diffusion coefficient determined for the discrete, merged, and continuous NSs were 6.16×10^{-11}, 2.08×10^{-12}, and 3.75×10^{-13} cm^2/s, respectively. Larger diffusion coefficient values were obtained from the chloroform-treated NSs of 5.11×10^{-8}, 1.04×10^{-9}, and 1.25×10^{-10} cm^2/s, respectively. The proton diffusion was improved after removal of the adsorbed ligand. The highest value of 2.60×10^{-7} mol/cm^2 for the chloroform-rinsed discrete NSs showed that the fast reaction rate benefited from the large active surface site exposure of the ultrathin 2D morphology. The above results for ECSA, the surface coverage of redox species, and the proton diffusion coefficient demonstrated that the chemisorbed ligand-modified $Ni(OH)_2$ NSs were highly active electrocatalysts in alkaline solutions. Compared to the adsorbed ligands, the chemisorbed ligand formed an alcoholophilic layer without impeding the activity sites. In addition, physisorbed ligand removal further promoted the NS activity by increasing the active sites and enhancing charge transfer.

CONCLUSIONS

In summary, we have synthesized a series of ultrathin 2D $Ni(OH)_2$ NSs with different morphologies and caps with different types of surface ligands. All of the NSs demonstrated a highly efficient EOR catalytic performance, where the largest improvements were obtained from discrete $Ni(OH)_2$ NSs. It showed an EOR onset potential of 1.4 V vs RHE and an overpotential of 230 mV at 10 mA cm^{-2}. The highest performance was obtained at 1.78 V with a current density of 107.7 mA cm^{-2}. The improvement was attributed to the chemisorbed $ODAM_{chem}$ ligands. Due to the alcoholophilic surface chemical environment created by the $ODAM_{chem}$ layer, the EOR kinetics are more favorable than those of the OER in alkaline electrolytes, with faster alcohol diffusion and adsorption rates onto the catalyst surface. We also showed that chloroform can remove the passive $ODAM_{ads}$ ligands on $Ni(OH)_2$ NSs and further boost the EOR activity to 163.8 mA cm^{-2} at 1.94 V. We will keep exploring better surfactant head groups for ILE NS growth to provide a stabler alcoholophilic layer for reliable long-term operation. This study provides a promising opportunity for the development of highly effective and low-cost electrocatalysts through a 2D geometry and surface ligand modifications, which may substantially improve the efficiency of alcohol oxidation and other organic electrocatalytic reactions. It could give fundamental insights into surface-related kinetics for a broad range of energy and environmental applications.

METHODS

Synthesis of $Ni(OH)_2$ NSs. The discrete $Ni(OH)_2$ NSs were synthesized using the ILE method. A 10 mL aqueous solution containing 2.5 mM nickel(II) chloride ($NiCl_2$) and 2 mM tartrate (Tart) was prepared in a 20 mL glass vial (with an inner diameter of 24 mm) by subsequently dissolving ammonium L-tartrate (Sigma-Aldrich) and $NiCl_2 \cdot 6H_2O$ (Sigma-Aldrich) powders. Then, 4 μL of a chloroform solution containing 1.8 mM octadecylamine (ODAM, Sigma-Aldrich) was slowly added onto the precursor solution surface. Finally, this glass vial was kept under ambient conditions for 4 h. The $Ni(OH)_2$ NSs could be transferred onto an arbitrary substrate by scooping at the surface of the solution or extracting the solution from the bottom of the vial for characterization and device fabrication. Si substrates were used for NS characterizations. To synthesize the merged $Ni(OH)_2$ NSs, $NiCl_2$ and tartrate concentrations were increased to 5 and 4 mM, respectively, with the other synthesis parameters being the same. Based on the parameters for the merged NSs, the ODAM solution amount was increased to 12 μL to facilitate the NSs fully merging into a continuous film, and the synthesis time was elongated to 6 h.

$Ni(OH)_2$ NS Characterizations. A Zeiss LEO 1530 field-emission scanning electron microscope (FESEM) was used to study the morphologies of the $Ni(OH)_2$ NSs. Atomic force microscopy (AFM) tomography images were obtained by using an XE-70 Park System. X-ray photoelectron spectroscopy (XPS) was obtained with a Thermo Scientific K-alpha XPS instrument at a 400 μm spot size with the flood gun turned on during the measurements. An *in situ* grazing incidence X-ray diffraction (GID) experiment was performed at beamline 15-ID-C ChemMatCARS at the Advanced Photon Source (APS) at Argonne National Laboratory. A 100 mL precursor solution was prepared in a Teflon trough with a 60 cm^2 open area (6 cm × 10 cm), and 53.5 μL of ODAM solution was added onto the surface to achieve the same surfactant density as the growth with 4 μL in a 20 mL glass vial.

Electrode Preparation. All working electrodes were prepared on fluorine-doped tin oxide (FTO) substrates with an exposed area of 1 cm^2. $Ni(OH)_2$ NSs for electrochemical measurements were directly transferred to FTO substrates by scooping at the air−water interface. The electrochemically deposited $Ni(OH)_2$ film was prepared by galvanostatically maintaining a current density of −0.25 mA cm^{-2} for 45 s in an aqueous plating solution containing 10 mM $Ni(NO_3)_2 \cdot 6H_2O$ and 30 mM KNO_3. The resulting $Ni(OH)_2$ films were rinsed with DI water and then dried in air at room temperature.

Electrochemical Measurements. The electrochemical measurements were performed on an Autolab PGSTAT302N station, using a three-electrode setup, with $Ni(OH)_2$ NSs on the FTO substrate as the working electrode, a Pt wire as the counter electrode, and a saturated calomel electrode (E_{SCE} = 0.241 V) as the reference electrode. The potential was swept from the open circuit in the positive direction at a scan rate of 50 mV s^{-1} for CVs.

Product Analysis. Quantification of electrolysis products of the ethanol oxidation was achieved via ^{1}H NMR spectroscopy using a Bruker Avance III 400 MHz NMR spectrometer. NMR samples were prepared by placing 0.2 mL of the electrolysis solution and 0.3 mL of D_2O in a 7 in. NMR tube and shaking vigorously. Product quantification was performed by comparing the product integration in the postelectrolysis solutions to those prepared with known concentrations.

Active Site Analysis. The ECSAs of all of $Ni(OH)_2$ NSs were determined by the double-layer capacitance (C_{dl}) from CV measurements at several scan rates (0.01−0.05 V s^{-1}) in the range −0.15 to +0.05 V vs SCE (0.92−1.12 V vs RHE; in the non-Faradaic region) in 1 M KOH solution. C_{dl} was calculated from the slope of the plot of the double-layer charging current (i_{dl}, mA) vs the scan rate (ν, V s^{-1}).[58] The ECSA was calculated by the equation ECSA = C_{dl}/C_S, where C_S is the specific capacitance of the samples. Herein, a C_S value of 0.040 mF cm^{-2} was used according to the previously reported value of metal oxide/hydroxides in an alkaline solution.[59] CV measurements were performed at different scan rates (0.01−0.05 V s^{-1}) in the range

https://doi.org/10.1021/acsnano.3c05014
ACS Nano 2023, 17, 17180−17189

0.15−0.45 V vs SCE (1.22−1.52 V vs RHE) in 1 M KOH solution to estimate the surface coverage of Ni^{2+}/Ni^{3+} redox species and proton diffusion coefficient. The surface coverage of redox species (Γ) was calculated from the slope of the linear fitting of the anodic peak current with the scan rate, by using the equation[53] $I = \left(\frac{n^2F^2}{4RT}\right)A\Gamma\nu$, where I is the peak current, n is the number of transferred electrons (n = 1 for Ni^{2+}/Ni^{3+}), F is the Faraday constant (96845 C/mol), R is the Boltzmann constant (8.314 J/(K mol)), T is the temperature (298 K), A is the area of the electrode (1 cm^2), and ν is the scan rate. The proton diffusion coefficient (D) was calculated from the slope of the linear fitting of the anodic peak current with the square root of the scan rate, by using the Randles−Sevcik equation,[53] $I = (2.69 \times 10^5)n^{3/2}AD^{1/2}C\nu^{1/2}$, where I is the peak current, n is the number of transferred electrons (n = 1 for Ni^{2+}/Ni^{3+}), A is the area of the electrode (1 cm^2), C is the proton concentration (0.043 mol/cm^3),[57] and ν is the scan rate.

ASSOCIATED CONTENT

Supporting Information

(PDF) The Supporting Information is available free of charge at https://pubs.acs.org/doi/10.1021/acsnano.3c05014.

Additional experimental results, SEM images, XPS spectra, CV plots, and NMR spectra (PDF)

EOR performance of discrete $Ni(OH)_2$ NSs at the beginning, Video S1, nn3c05014_si_002.mp4 (MP4)

EOR performance of discrete $Ni(OH)_2$ NSs after 4 hours, Video S2, nn3c05014_si_003.mp4 (MP4)

AUTHOR INFORMATION

Corresponding Author

Xudong Wang − *Department of Materials Science and Engineering, University of Wisconsin-Madison, Madison, Wisconsin 53706, United States;* orcid.org/0000-0002-9762-6792; Email: xudong.wang@wisc.edu

Authors

Ziyi Zhang − *Department of Materials Science and Engineering, University of Wisconsin-Madison, Madison, Wisconsin 53706, United States;* orcid.org/0000-0001-9102-8292

Yutao Dong − *Department of Materials Science and Engineering, University of Wisconsin-Madison, Madison, Wisconsin 53706, United States;* orcid.org/0000-0003-3582-087X

Corey Carlos − *Department of Materials Science and Engineering, University of Wisconsin-Madison, Madison, Wisconsin 53706, United States;* orcid.org/0000-0002-9398-2554

Complete contact information is available at: https://pubs.acs.org/10.1021/acsnano.3c05014

Notes

The authors declare no competing financial interest.

ACKNOWLEDGMENTS

This work was primarily supported by the National Science Foundation (DMR-2114931). GID data were collected at NSF's ChemMatCARS Sector 15, which was principally supported by the Divisions of Chemistry (CHE) and Materials Research (DMR), National Science Foundation, under Grant NSF/CHE-1834750. The use of the Advanced Photon Source, an Office of Science User Facility operated for the U.S. Department of Energy (DOE) Office of Science by Argonne National Laboratory, was supported by the U.S. DOE under Contract DE-AC02-06CH11357.

REFERENCES

(1) Chu, S.; Majumdar, A. Opportunities and challenges for a sustainable energy future. *Nature* **2012**, *488*, 294−303.

(2) Zhao, X.; et al. Two-dimensional electrocatalysts for alcohol oxidation: A critical review. *Chemical Engineering Journal* **2020**, *400*, No. 125744.

(3) Bender, M. T.; Yuan, X.; Choi, K.-S. Alcohol oxidation as alternative anode reactions paired with (photo) electrochemical fuel production reactions. *Nat. Commun.* **2020**, *11*, 4594.

(4) Fu, X.; Wan, C.; Huang, Y.; Duan, X. Noble metal based electrocatalysts for alcohol oxidation reactions in alkaline media. *Adv. Funct. Mater.* **2022**, *32*, 2106401.

(5) Lv, H.; Sun, L.; Wang, Y.; Liu, S.; Liu, B. Highly Curved, Quasi-Single-Crystalline Mesoporous Metal Nanoplates Promote C−C Bond Cleavage in Ethanol Oxidation Electrocatalysis. *Adv. Mater.* **2022**, *34*, 2203612.

(6) Wang, H.; et al. PdBi single-atom alloy aerogels for efficient ethanol oxidation. *Adv. Funct. Mater.* **2021**, *31*, 2103465.

(7) Luo, S.; et al. A tensile-strained Pt−Rh single-atom alloy remarkably boosts ethanol oxidation. *Adv. Mater.* **2021**, *33*, 2008508.

(8) Shang, H.; et al. General synthesis of Pd−pm (pm= Ga, In, Sn, Pb, Bi) alloy nanosheet assemblies for advanced electrocatalysis. *Nanoscale* **2020**, *12*, 3411−3417.

(9) Qiu, Y.; et al. Construction of Pd-Zn dual sites to enhance the performance for ethanol electro-oxidation reaction. *Nat. Commun.* **2021**, *12*, 5273.

(10) Gao, F.; Zhang, Y.; Ren, F.; Shiraishi, Y.; Du, Y. Universal surfactant-free strategy for self-standing 3D tremella-like Pd−M (M= Ag, Pb, and Au) nanosheets for superior alcohols electrocatalysis. *Adv. Funct. Mater.* **2020**, *30*, 2000255.

(11) Yun, Q.; et al. Synthesis of PdM (M= Zn, Cd, ZnCd) nanosheets with an unconventional face-centered tetragonal phase as highly efficient electrocatalysts for ethanol oxidation. *ACS Nano* **2019**, *13*, 14329−14336.

(12) Zhou, X.; et al. Preparation of Au@Pd Core−Shell Nanorods with fcc-2H-fcc Heterophase for Highly Efficient Electrocatalytic Alcohol Oxidation. *J. Am. Chem. Soc.* **2022**, *144*, 547.

(13) Zhu, Y.; Bu, L.; Shao, Q.; Huang, X. Subnanometer PtRh nanowire with alleviated poisoning effect and enhanced C−C bond cleavage for ethanol oxidation electrocatalysis. *ACS Catal.* **2019**, *9*, 6607−6612.

(14) Wang, Y.; et al. p−d Orbital hybridization induced by a monodispersed Ga site on a Pt3Mn nanocatalyst boosts ethanol electrooxidation. *Angew. Chem., Int. Ed.* **2022**, *61*, No. e202115735.

(15) Shen, C.; et al. Introducing oxophilic metal and interstitial hydrogen into the Pd lattice to boost electrochemical performance for alkaline ethanol oxidation. *Journal of Materials Chemistry A* **2022**, *10*, 1735−1741.

(16) Wang, X.; et al. Materializing efficient methanol oxidation via electron delocalization in nickel hydroxide nanoribbon. *Nat. Commun.* **2020**, *11*, 4647.

(17) Bender, M. T.; Lam, Y. C.; Hammes-Schiffer, S.; Choi, K.-S. Unraveling two pathways for electrochemical alcohol and aldehyde oxidation on NiOOH. *J. Am. Chem. Soc.* **2020**, *142*, 21538−21547.

(18) Bender, M. T.; Warburton, R. E.; Hammes-Schiffer, S.; Choi, K.-S. Understanding hydrogen atom and hydride transfer processes during electrochemical alcohol and aldehyde oxidation. *ACS Catal.* **2021**, *11*, 15110−15124.

(19) Francàs, L.; et al. Spectroelectrochemical study of water oxidation on nickel and iron oxyhydroxide electrocatalysts. *Nat. Commun.* **2019**, *10*, 5208.

(20) Ding, Y.; et al. Hydrogen and potassium acetate co-production from electrochemical reforming of ethanol at ultrathin cobalt sulfide nanosheets on nickel foam. *ACS Appl. Mater. Interfaces* **2021**, *13*, 4026−4033.

(21) Liu, C.; et al. Air-Assisted Transient Synthesis of Metastable Nickel Oxide Boosting Alkaline Fuel Oxidation Reaction. *Adv. Energy Mater.* **2020**, *10*, No. 2001397.
(22) Goetz, M. K.; Bender, M. T.; Choi, K.-S. Predictive control of selective secondary alcohol oxidation of glycerol on NiOOH. *Nat. Commun.* **2022**, *13*, 5848.
(23) Wu, X.; et al. Emerging 2D materials for electrocatalytic applications: synthesis, multifaceted nanostructures, and catalytic center design. *Small* **2022**, *18*, 2105831.
(24) Wang, Y.; Zhang, Z.; Mao, Y.; Wang, X. Two-dimensional nonlayered materials for electrocatalysis. *Energy Environ. Sci.* **2020**, *13*, 3993−4016.
(25) Wang, F.; et al. Nanometre-thick single-crystalline nanosheets grown at the water−air interface. *Nat. Commun.* **2016**, *7*, 1−7.
(26) Wang, Y.; et al. Bioinspired Synthesis of Quasi-Two-Dimensional Monocrystalline Oxides. *Chem. Mater.* **2019**, *31*, 9040−9048.
(27) Zhang, Z.; et al. Nucleation Kinetics and Structure Evolution of Quasi-Two-Dimensional ZnO at the Air-Water Interface: An In Situ Time-Resolved Grazing Incidence X-ray Scattering Study. *Nano Lett.* **2022**, *22*, 3040−3046.
(28) Konavarapu, S. K.; Ghosh, D.; Dey, A.; Pradhan, D.; Biradha, K. Isostructural NiII Metal−Organic Frameworks (MOFs) for Efficient Electrocatalysis of Oxygen Evolution Reaction and for Gas Sorption Properties. *Chemistry A European Journal* **2019**, *25*, 11141−11146.
(29) Li, Y.; et al. Rattle-structured CuO/Co3O4@C microspheres, a potent bifunctional catalyst for hydrogen production from ammonia borane hydrolysis and methanolysis. *Appl. Surf. Sci.* **2023**, *636*, No. 157840.
(30) Williams, C. K.; Lashgari, A.; Chai, J.; Jiang, J. J. Enhanced Molecular CO2 Electroreduction Enabled by a Flexible Hydrophilic Channel for Relay Proton Shuttling. *ChemSusChem* **2020**, *13*, 3412−3417.
(31) Yan, G.; et al. Nanoparticle-Decorated Ultrathin La2O3 Nanosheets as an Efficient Electrocatalysis for Oxygen Evolution Reactions. *Nano-Micro Letters* **2020**, *12*, 49.
(32) Zhao, Y.; et al. Quasi-Two-Dimensional Earth-Abundant Bimetallic Electrocatalysts for Oxygen Evolution Reactions. *ACS Energy Letters* **2021**, *6*, 3367−3375.
(33) Yin, X.; et al. Ionic Layer Epitaxy of Nanometer-Thick Palladium Nanosheets with Enhanced Electrocatalytic Properties. *Chem. Mater.* **2018**, *30*, 3308−3314.
(34) Wang, F.; Yin, X.; Wang, X. Morphological control in the adaptive ionic layer epitaxy of ZnO nanosheets. *Extreme Mechanics Letters* **2016**, *7*, 64−70.
(35) Yin, X.; et al. Unit cell level thickness control of single-crystalline zinc oxide nanosheets enabled by electrical double-layer confinement. *Langmuir* **2017**, *33*, 7708−7714.
(36) Zhang, Z.; et al. Nucleation Kinetics and Structure Evolution of Quasi-Two-Dimensional ZnO at the Air−Water Interface: An In Situ Time-Resolved Grazing Incidence X-ray Scattering Study. *Nano Lett.* **2022**, *22*, 3040−3046.
(37) Janusz, W.; Skwarek, E. Comparison of oxalate, citrate and tartrate ions adsorption in the hydroxyapatite/aqueous electrolyte solution system. *Colloids and Interfaces* **2020**, *4*, 45.
(38) Neveu, S.; Bee, A.; Robineau, M.; Talbot, D. Size-selective chemical synthesis of tartrate stabilized cobalt ferrite ionic magnetic fluid. *J. Colloid Interface Sci.* **2002**, *255*, 293−298.
(39) Owen, J. The coordination chemistry of nanocrystal surfaces. *Science* **2015**, *347*, 615−616.
(40) Cappus, D.; et al. Polar surfaces of oxides: reactivity and reconstruction. *Surf. Sci.* **1995**, *337*, 268−277.
(41) Zhang, H.; et al. Facet-dependent rock-salt reconstruction on the surface of layered oxide cathodes. *Chem. Mater.* **2018**, *30*, 692−699.
(42) Payne, B. P. *X-ray Photoelectron Spectroscopy Studies on the Oxidation Processes of Nickel, Chromium and their Alloys*; The University of Western Ontario (Canada): 2011.
(43) Wang, W.; et al. Self-healing performance and corrosion resistance of graphene oxide−mesoporous silicon layer−nanosphere structure coating under marine alternating hydrostatic pressure. *Chemical Engineering Journal* **2019**, *361*, 792−804.
(44) Sharel, P.; et al. Electrodeposition of nickel hydroxide nanoparticles on carbon nanotube electrodes: correlation of particle crystallography with electrocatalytic properties. *J. Phys. Chem. C* **2016**, *120*, 16059−16068.
(45) Bender, M. T.; Choi, K.-S. Electrochemical Dehydrogenation Pathways of Amines to Nitriles on NiOOH. *JACS Au* **2022**, *2*, 1169−1180.
(46) Fleischmann, M.; Korinek, K.; Pletcher, D. The kinetics and mechanism of the oxidation of amines and alcohols at oxide-covered nickel, silver, copper, and cobalt electrodes. *J. Chem. Soc., Perkin Trans.* **1972**, *2*, 1396−1403.
(47) Ma, W.; Wang, L.; Xue, J.; Cui, H. A bottom-up strategy for exfoliation-free synthesis of soluble α-Ni(OH)2 monolayer nanosheets on a large scale. *RSC Adv.* **2016**, *6*, 85367−85373.
(48) Wang, D.; et al. Morphology-controlled synthesis of hierarchical mesoporous α-Ni(OH)2 microspheres for high-performance asymmetric supercapacitors. *J. Alloys Compd.* **2018**, *737*, 238−247.
(49) Cai, J.; et al. Robust construction of flexible bacterial cellulose@ Ni (OH) 2 paper: toward high capacitance and sensitive H2O2 detection. *Engineered Science* **2019**, *5*, 21−29.
(50) Chang, Y.-H.; Liu, C.; Feng, S.-P. Electrochemical fabrication of metal nanostructures by using a hydrophilic/hydrophobic sponge-like NiOOH/Ni(OH)2 template. *Thin Solid Films* **2016**, *603*, 1−7.
(51) Lu, J.; et al. Hydrophilic Ni(OH)2@CoB nano-chains with shell-core structure as an efficient catalyst for oxygen evolution reaction. *J. Alloys Compd.* **2020**, *844*, No. 156129.
(52) Klaus, S.; Cai, Y.; Louie, M. W.; Trotochaud, L.; Bell, A. T. Effects of Fe Electrolyte Impurities on Ni(OH)2/NiOOH Structure and Oxygen Evolution Activity. *J. Phys. Chem. C* **2015**, *119*, 7243−7254.
(53) Bard, A. J.; Faulkner, L. R.; White, H. S. *Electrochemical methods: fundamentals and applications*; Wiley: 2022.
(54) Dubale, A. A.; et al. High-Performance Bismuth-Doped Nickel Aerogel Electrocatalyst for the Methanol Oxidation Reaction. *Angew. Chem., Int. Ed.* **2020**, *59*, 13891−13899.
(55) Hao, Y.; et al. Methanol upgrading coupled with hydrogen product at large current density promoted by strong interfacial interactions. *Energy Environ. Sci.* **2023**, *16*, 1100−1110.
(56) Li, J.; et al. Selective methanol-to-formate electrocatalytic conversion on branched nickel carbide. *Angew. Chem.* **2020**, *132*, 21012−21016.
(57) Zhang, S.-J.; Zheng, Y.-X.; Yuan, L.-S.; Zhao, L.-H. Ni−B amorphous alloy nanoparticles modified nanoporous Cu toward ethanol oxidation in alkaline medium. *J. Power Sources* **2014**, *247*, 428−436.
(58) McCrory, C. C. L.; et al. Benchmarking Hydrogen Evolving Reaction and Oxygen Evolving Reaction Electrocatalysts for Solar Water Splitting Devices. *J. Am. Chem. Soc.* **2015**, *137*, 4347−4357.
(59) McCrory, C. C. L.; Jung, S.; Peters, J. C.; Jaramillo, T. F. Benchmarking Heterogeneous Electrocatalysts for the Oxygen Evolution Reaction. *J. Am. Chem. Soc.* **2013**, *135*, 16977−16987.

https://doi.org/10.1021/acsnano.3c05014
ACS Nano 2023, 17, 17180−17189